Activity-based photoacoustic probe for biopsy-free assessment of copper in murine models of Wilson's disease and liver metastasis

Melissa Y. Lucero[a], Yuqi Tang[a], Chloe J. Zhang[a], Shengzhang Su[a], Joseph A. Forzano[a], Valeria Garcia[a], Xin Huang[a], David Moreno[a], and Jefferson Chan[a,1]

[a]Department of Chemistry, The Beckman Institute for Advanced Science and Technology, University of Illinois at Urbana–Champaign, Urbana, IL 61801

Edited by Christopher J. Chang, University of California, Berkeley, CA, and accepted by Editorial Board Member Stephen J. Benkovic August 5, 2021 (received for review April 12, 2021)

The development of high-performance photoacoustic (PA) probes that can monitor disease biomarkers in deep tissue has the potential to replace invasive medical procedures such as a biopsy. However, such probes must be optimized for in vivo performance and exhibit an exceptional safety profile. In this study, we have developed PACu-1, a PA probe designed for biopsy-free assessment (BFA) of hepatic Cu via photoacoustic imaging. PACu-1 features a Cu(I)-responsive trigger appended to an aza-BODIPY dye platform that has been optimized for ratiometric sensing. Owing to its excellent performance, we were able to detect basal levels of Cu in healthy wild-type mice as well as elevated Cu in a Wilson's disease model and in a liver metastasis model. To showcase the potential impact of PACu-1 for BFA, we conducted two blind studies in which we were able to successfully identify Wilson's disease animals from healthy control mice in each instance.

photoacoustic imaging | copper | Wilson's disease

Photoacoustic (PA) imaging is a light-in, sound-out technique that has emerged as a promising biomedical approach for the noninvasive assessment of various ailments in humans, ranging from arthritis to cancer (1, 2). Excitation of an endogenous pigment such as hemoglobin in blood or melanin in tissue can provide contrast, since relaxation via nonradiative decay can trigger thermoelastic expansion of the surrounding tissue. Repeatedly irradiating a region of interest with a pulsed laser can result in pressure waves that can be readily detected by ultrasound transducers. Since ultrasound at clinically relevant frequencies can travel through the body with minimal perturbation, it is possible to accurately pinpoint the source of the signal to afford high-resolution images at centimeter imaging depths (3). Beyond label-free applications, the utility of PA imaging for disease detection has been augmented by the recent development of acoustogenic probes (activatable PA probes) that give an off-on signal enhancement or ratiometric readout (4, 5). Such examples, as well as imaging agents for other modalities, are designed based on the principles of activity-based sensing, which leverages the chemical reactivity of an analyte to probe and manipulate the system under investigation (6–8). Notable acoustogenic molecules include those that can visualize dysregulated enzymatic activities (9–12), properties of the disease tissue microenvironment (13–15), as well as small molecule– and metal ion–based disease biomarkers (16–24). However, replacing an invasive medical procedure, such as a liver biopsy, with an acoustogenic probe is an immense challenge, since the in vivo performance and safety profile of such a chemical tool must be exceptional. Thus, despite undesirable shortcomings, such as the potential to develop severe infections, false negatives due to collection of nondiseased tissue, and the inability to directly monitor disease progression in real time (25), liver biopsies are still commonly employed to assess biomarkers in conditions such as Wilson's disease (WD) (26) and cancer (27).

It is noteworthy that elevated levels of hepatic copper (Cu) are a common biomarker shared by these conditions. In WD, Cu accumulates in the liver due to a genetic mutation in the Cu exporter, ATP7B, and this can lead to chronic liver damage, which can become fatal if not treated (28, 29). In the context of cancer, Cu is elevated in many solid tumors including breast (30, 31) and lung (32, 33) cancers, which generally metastasize to the liver. Since Cu can promote angiogenesis and drive tumor progression, biopsy-free assessment (BFA) of Cu in metastatic lesions is critical. A number of Cu probes exists for various modalities (34, 35), including examples compatible with in vivo applications via fluorescent (36) and bioluminescent (37) imaging. However, approaches that involve the emission of photons are more suitable for shallow imaging depths (millimeter range) owing to scattering and attenuation of light. More recently, our group (16, 38) and others (39) have developed Cu probes for PA imaging to achieve greater tissue penetration and higher resolution. However, these probes are designed to target Cu(II), whereas intracellular Cu exists predominantly in the +1 form owing to the highly reducing environment of the cell (40). To overcome this challenge, we present the development of PACu-1, an acoustogenic probe for Cu(I), and its application in BFA of hepatic Cu in a WD model and a liver metastasis model. Moreover, we designed two unbiased BFA blind studies to identify WD mice from healthy wild-type (WT) controls using PACu-1.

Significance

The ability to noninvasively detect and track disease biomarkers via photoacoustic imaging (a light-in, sound-out technique) can potentially substitute invasive medical procedures such as a liver biopsy. While achieving this goal can have a profound impact on disease management, it is an immense challenge that requires novel chemical tools that are sensitive, selective, and safe. Here, we report a photoacoustic probe designed for Cu(I), which becomes dysregulated in many disease states. In addition to demonstrating in vivo efficacy in multiple models, we designed two blind studies to assess its utility for biopsy-free assessment of hepatic copper levels in Wilson's disease. This work sets the stage for future studies to evaluate the performance of photoacoustic probe designs for biomedical applications.

Author contributions: M.Y.L. and J.C. designed research; M.Y.L., Y.T., C.J.Z., S.S., J.A.F., V.G., X.H., and D.M. performed research; M.Y.L. and J.C. analyzed data; and M.Y.L. and J.C. wrote the paper.

The authors declare no competing interest.

This article is a PNAS Direct Submission. C.J.C. is a guest editor invited by the Editorial Board.

[1]To whom correspondence may be addressed. Email: jeffchan@illinois.edu.

This article contains supporting information online at https://www.pnas.org/lookup/suppl/doi:10.1073/pnas.2106943118/-/DCSupplemental.

Published September 3, 2021.

Results

Design and Characterization of PACu-1. To target the +1 oxidation state of Cu, we installed a Cu(I)-responsive tris[(2-pyridyl)methyl] amine (TPA) (41) trigger onto an optimized aza-BODIPY dye platform to yield PACu-1, which features ratiometric imaging capabilities. Specifically, we hypothesized that capping of the 2,6-dichlorophenol moiety will result in a blue shift of the wavelength of maximum absorbance (λ_{max}) relative to the uncapped probe. However, the binding of Cu(I) to TPA [to form an initial Cu(I)–PACu-1 tetrahedral complex] will induce an oxidative cleavage event of the pendant ether linkage to release the latent dye and Cu(II)–TPA, which changes to a trigonal bipyramidal geometry (Fig. 1*A* and *SI Appendix*, Fig. S1) (42, 43). Selective irradiation of each form (probe and product) at their corresponding λ_{max} will yield two signals, from which a ratio can be determined. This probe design feature is important for BFA, especially in the liver, since we anticipate there to be significant background interference from blood. In addition, we selected the aza-BODIPY platform to develop PACu-1 due to their large extinction coefficients (10^4 to 10^5 $M^{-1} \cdot cm^{-1}$) in the near infrared range and low fluorescence quantum yields, since both of these properties translate to a stronger PA signal (38). Lastly, we have determined empirically that many of the aza-BODIPY–based probes we have developed intrinsically localize to the liver owing to its relatively high hydrophobic properties (44).

After synthesizing PACu-1 (*SI Appendix*, Scheme 1), we evaluated its in vitro response to 20 equivalents of Cu(I) (introduced as $[Cu(CH_3CN)_4]PF_6$). After 1 h incubation at room temperature, we observed a large spectral shift of 91 nm from 678 nm (probe, $\varepsilon = 5.3 \times 10^4$ $M^{-1} \cdot cm^{-1}$) to 767 nm (product, $\varepsilon = 3.7 \times 10^4$ $M^{-1} \cdot cm^{-1}$) (Fig. 1*B*). Given that the extinction coefficient of a molecule is a reliable proxy for its PA output, we estimate the ratiometric turn-on will be ~10.4-fold [defined as $(770/680_{Final})/(770/680_{Initial})$]. Importantly, irradiation at 680 nm will predominately excite PACu-1, whereas light at 770 nm will only generate a signal that corresponds to the turned-over product (Fig. 1 *C*

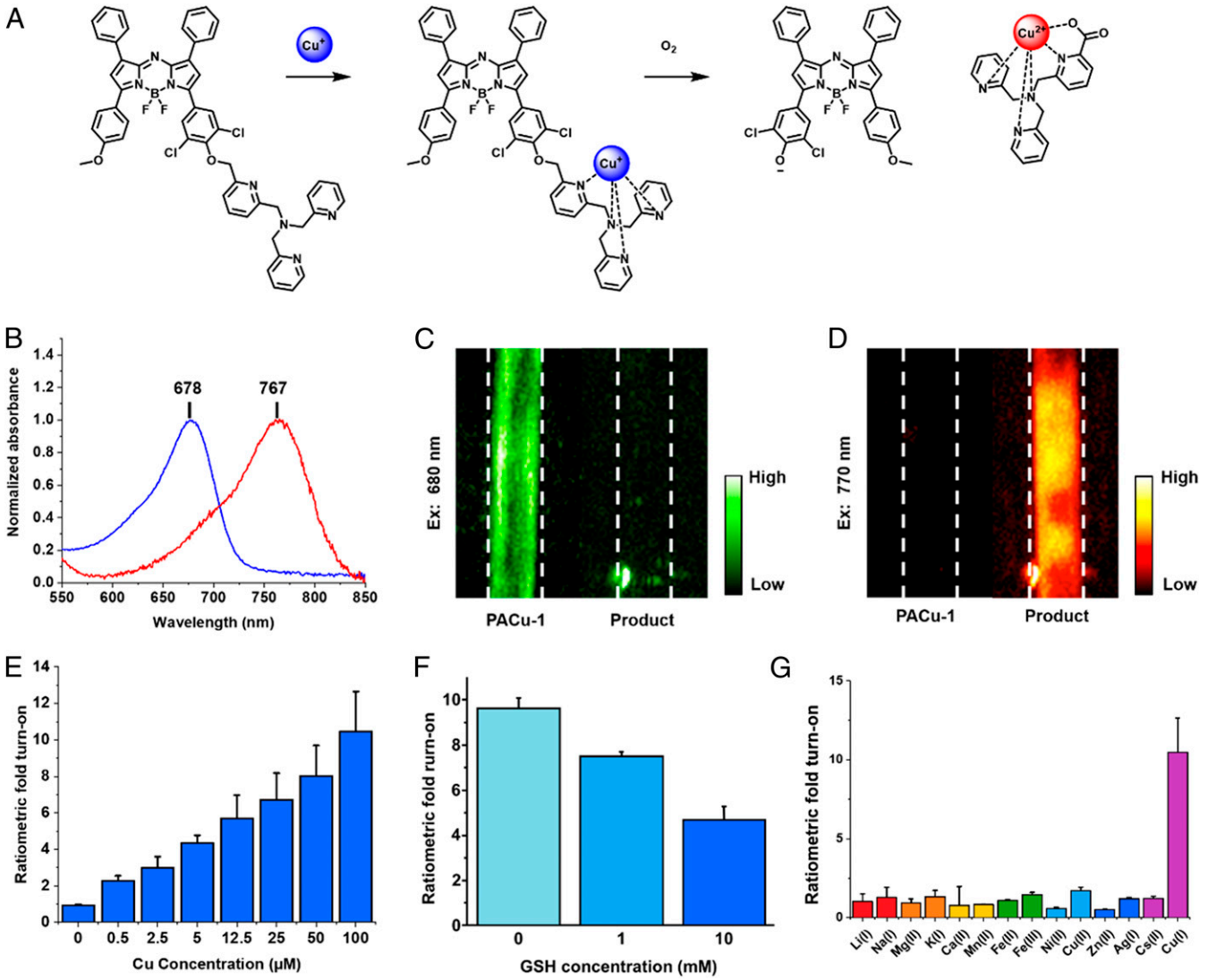

Fig. 1. (*A*) General reaction schematic of PACu-1 with Cu(I). (*B*) Normalized absorbance spectra of PACu-1 (blue) and turnover product (red). PA image of (*C*) PACu-1 and (*D*) the product in a tissue-mimicking phantom excited at 680 and 770 nm. Images compiled from different phantoms. (*E*) Ratiometric fold turn-on after incubating PACu-1 with 0, 0.5, 2.5, 5, 12.5, 25, 50, and 100 μM Cu(I). (*F*) Ratiometric fold turn-on of PACu-1 after incubating with 100 μM Cu(I) and 0, 1, or 10 mM GSH. (*G*) Ratiometric fold turn-on after incubating with 100 μM of various metal ions. The source of the Cu(I) used for all experiments was $[(CH_3CN)_4Cu]PF_6$. All assays were performed in 1:1 dimethylformamide:Hepes, pH 7.4 for 1 h. Values are reported as mean ± SD ($n = 3$).

and *D*). Moreover, we were able to observe a dose-dependent response to Cu (LOD = 0.2 μM) (Fig. 1*E*). We were also able to show that PACu-1 can function in the presence of glutathione (GSH), an abundant biological thiol that can compete with PACu-1 to bind Cu(I) (Fig. 1*F*). Indeed, GSH is present at high levels in the liver and most solid tumors (up to 10 mM) (45, 46). To probe the oxygen dependency of the reaction, we employed the nitrogen purge technique (for 40 min) and found that PACu-1 could still turn over, albeit at a slower rate, when oxygen levels were reduced to 0.2 to 0.4 ppm (*SI Appendix*, Fig. S2) (47). Lastly, PACu-1 was shown to exhibit excellent selectivity for Cu(I) against a panel of monovalent and divalent metal ions (Fig. 1*G*). In the presence of these metal ions, PACu-1 was shown to retain its reactivity toward Cu(I) (*SI Appendix*, Fig. S3). These findings are significant because in addition to Cu(I), the TPA trigger has been tuned to sense other metal ions and thus may exhibit off-target reactivity (48, 49).

Metabolic Stability, Biodistribution, and Safety Profile of PACu-1. Because our objective is to employ PACu-1 for BFA of hepatic Cu via PA imaging, it is critical to 1) demonstrate that it is not metabolized in the liver to give false positives and 2) show that it is biocompatible with an excellent safety profile. To this end, we treated PACu-1 with rat liver microsomes rich in metabolic enzymes (e.g., Cytochrome P450s). After an incubation period of 1 h, we did not observe any change in the absorbance spectra indicating there would be minimal off-target activation of PACu-1 that can lead to false positive results (*SI Appendix*, Fig. S4). We corroborated these results with mass spectroscopy analysis that showed that the latent aza-BODIPY was not being released (*SI Appendix*, Fig. S5). Next, we performed MTT (3-(4,5-dimethylthiazol-2-yl)-2,5-diphenyl-2H-tetrazolium bromide) assays to assess the cytotoxicity of the probe in mammalian cell lines. Human embryonic kidney 293 cells incubated with up to 25 μM PACu-1 for 24 h were shown to have no significant loss of viability (Fig. 2*A*). Likewise, the turned-over product was also found to be not cytotoxic under these conditions (*SI Appendix*, Fig. S6). Next, we sought to determine the biodistribution of PACu-1 after systemic administration in BALB/c mice via ex vivo PA imaging analysis of the vital organs. Our data indicates that PACu-1 predominantly localizes to the liver and does not accumulate in the heart, kidneys, or spleen (*SI Appendix*, Fig. S7). Before PACu-1 could be considered further as a chemical tool for BFA applications, we examined its in vivo safety profile. First, we performed hematoxylin and eosin (H&E) staining on liver samples obtained from mice treated with either a vehicle control or PACu-1. Our results show that the nuclear staining patterns were identical, suggesting that PACu-1 is nontoxic (Fig. 2*B* and *SI Appendix*, Fig. S8). Second, we conducted a comprehensive liver function test to measure the levels of albumin, alkaline phosphatase, alanine aminotransferase, aspartate transaminase, bilirubin, blood urea nitrogen,

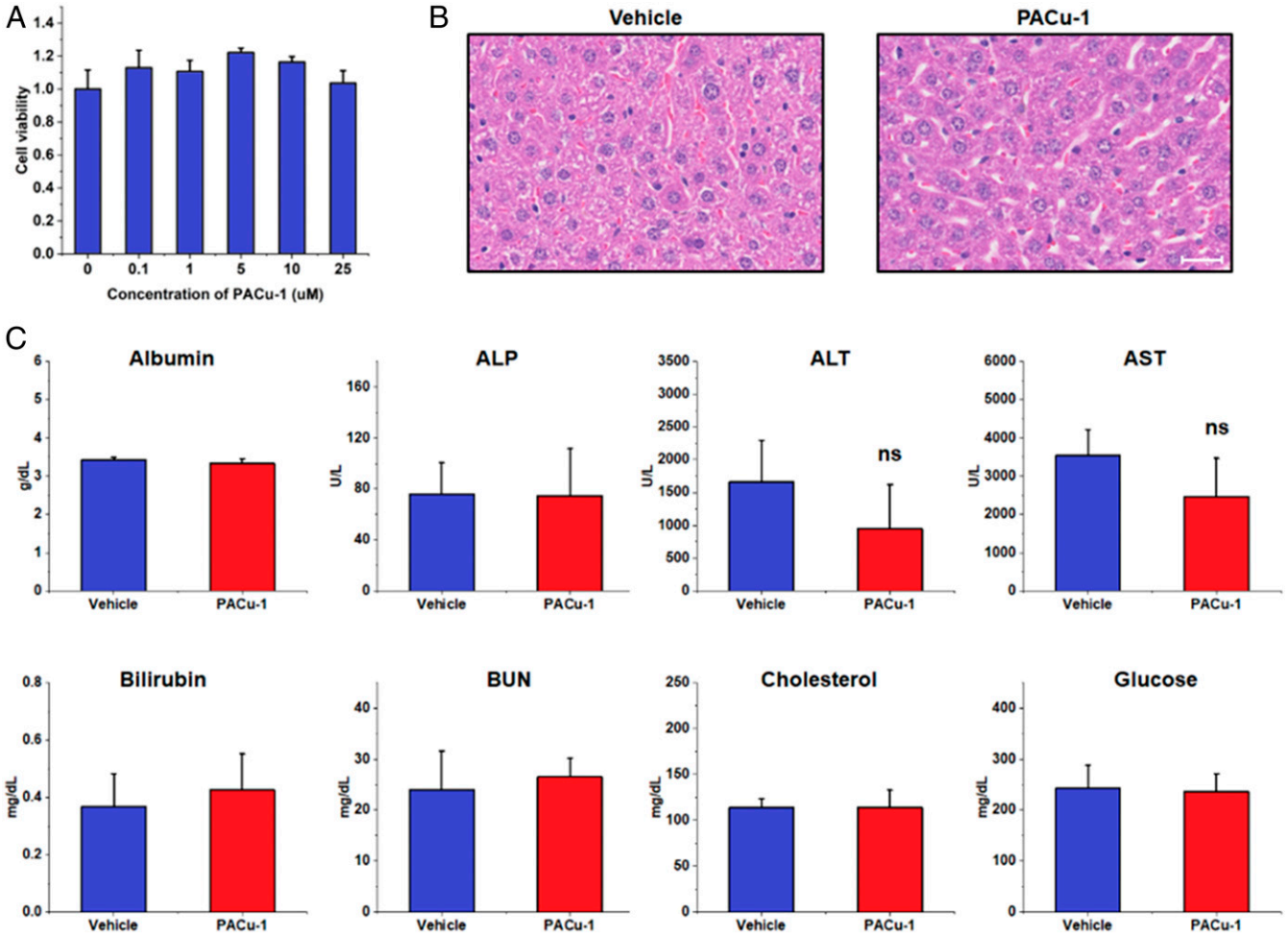

Fig. 2. (*A*) MTT assay measuring cell viability after incubating cells with 0, 0.1, 1, 5, 10, and 25 μM PACu-1 for 24 h. (*B*) H&E stains of the liver after treating live mice with 0 or 50 μM PACu-1. (Scale bar, 25 μm.) (*C*) Liver function assays on serum after treating live mice with 0 or 50 μM PACu-1. Values are reported as mean ± SD (n = 10). ALP, alkaline phosphatase; ALT, lanine aminotransferase; AST, aspartate aminotransferase; BUN, blood urea nitrogen.

cholesterol, and glucose in serum. We did not observe any statistical difference between vehicle- and PACu-1–treated animals, which further demonstrates that PACu-1 is safe and thus is suitable for BFA applications (Fig. 2*C*).

Imaging Exogenous Cu(I) in BALB/c Mice. Prior to determining whether PACu-1 can be employed to detect elevated hepatic Cu(I) in live animals, we treated BALB/c mice with $CuCl_2$ via intraperitoneal administration 2 h prior to isolating liver samples for ICP-MS (inductively coupled plasma mass spectrometry) analysis. Notably, Cu(II) is rapidly reduced to Cu(I) upon uptake into cells. Compared to animals that did not receive Cu supplementation (−Cu), the concentration of hepatic Cu was twice as high (Fig. 3*A*). We obtained similar results when PACu-1 was employed for PA imaging (Fig. 3 *B* and *C*). In particular, the $PA_{770/680}$ ratio was 1.48 ± 0.23 for the Cu-treated animals, whereas the corresponding ratio for control animals not treated with Cu was 0.94 ± 0.13 (Fig. 3*B*, red and blue bars, respectively). To confirm that these results were due to the detection of Cu(I), we coadministered ammonium tetrathiomolybdate (TM), a high-affinity Food and Drug Administration (FDA)-approved Cu chelator drug (K_d = $\sim 10^{-20}$) (50), with Cu. As anticipated, we did not observe any significant activation (0.94 ± 0.13) when TM was present, since it can outcompete PACu-1 for binding to Cu(I) (Fig. 3*B*, yellow bar). To further validate this finding, we administered Ctrl-PACu-1, a nonresponsive control probe that features an attenuated Cu(I) binding trigger (*SI Appendix*, Scheme 2), to a fourth group of animals pretreated with Cu. Interestingly, the $PA_{770/680}$ ratio (0.82 ± 0.12) was lower than when PACu-1 was employed to image animals not receiving Cu supplementation and the TM-treated group (Fig. 3*B*, green bar). This suggests that PACu-1 may be capable of detecting basal levels of Cu that are present in the liver.

PA Imaging of Hepatic Cu(I) in WD. Cu accumulation in the liver is a pathological hallmark of WD, which is typically assessed clinically via liver biopsies (51). Using an established ATP7B genetic knockout model of WD developed by Lutsenko and coworkers (JAX stock No. 032624), we measured the levels of hepatic Cu in WT mice and WD mice using ICP-MS analysis after obtaining biopsied tissue. On average, we found that the Cu levels in WD mice were 17.5-fold greater than WT mice (Fig. 4*A*). Likewise, when we employed PACu-1 and PA imaging for BFA of Cu, we found that the $PA_{770/680}$ ratio was significantly higher in WD mice (1.24 ± 0.16) relative to WT mice (0.80 ± 0.11) (Fig. 4 *B*–*D*). It is critical to note that while ICP-MS analysis reports on total Cu levels, PACu-1 can only access the labile pool, which is defined as Cu weakly associated with intracellular chelators such as GSH. To confirm the in vivo imaging results, we harvested the heart, kidneys, liver, and spleen from WD and WT mice treated with PACu-1 to perform ex vivo PA imaging. This experiment was performed to demonstrate that the PA signal intensity is higher in the liver of WD mice owing to activation of PACu-1 (*SI Appendix*, Fig. S9).

BFA of Hepatic Cu(I) in WD via Blind Studies. To evaluate the potential efficacy of PACu-1 for BFA of hepatic Cu(I) in WD, it is critical to perform a rigorous study that is free of potential bias.

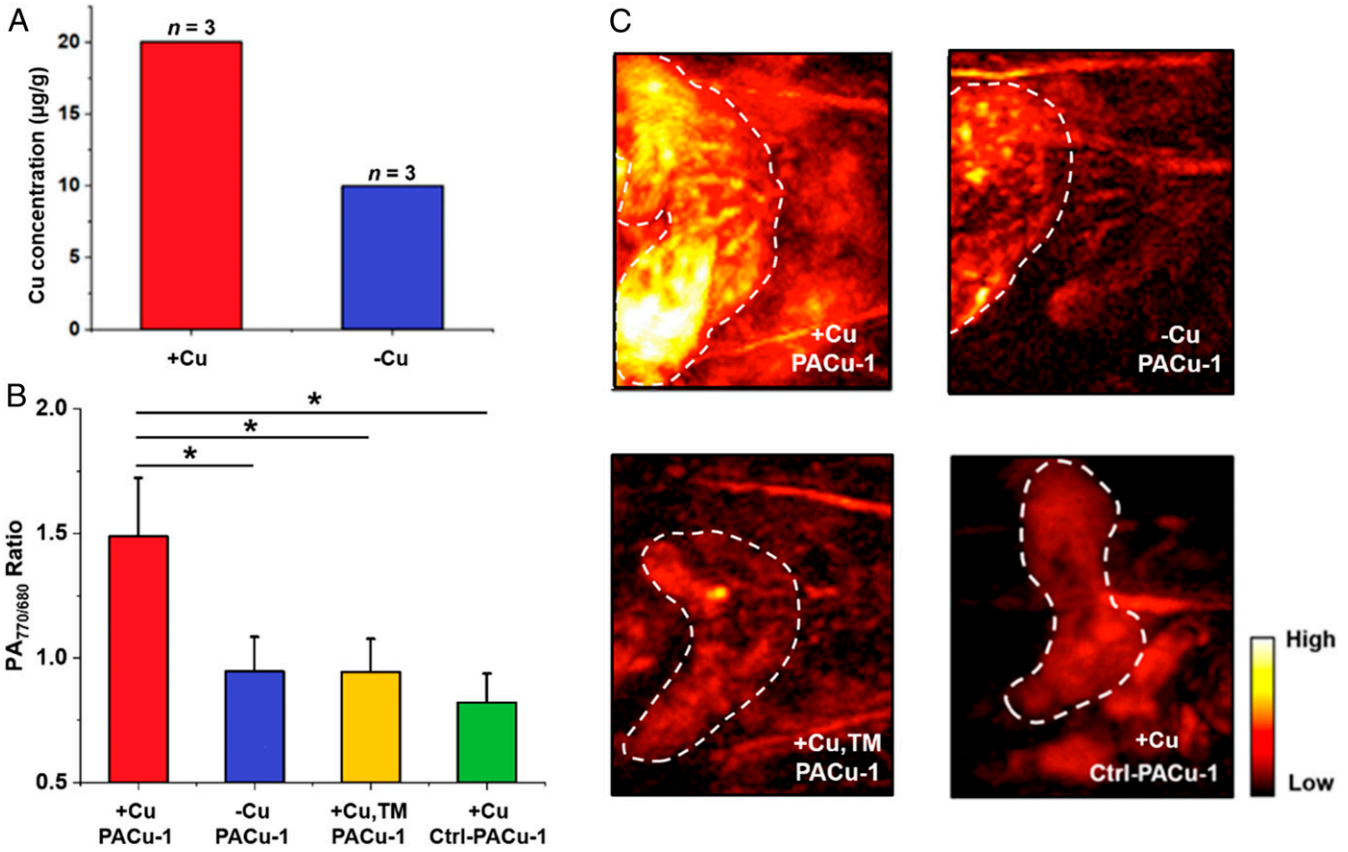

Fig. 3. (*A*) Cu concentration in the liver after pretreatment with 0 mg/kg $CuCl_2$ or 5 mg/kg $CuCl_2$ obtained via ICP-MS. (*B*) PA ratio obtained using PACu-1 (50 μM). Red bar represents pretreatment with 5 mg/kg $CuCl_2$ ($n = 4$). Blue bar represents pretreatment with 0 mg/kg $CuCl_2$ ($n = 5$). Yellow bar represents pretreatment with 5 mg/kg $CuCl_2$ and ammonium tetrathiomolybdate (TM) ($n = 5$). Green bar represents pretreatment with 5 mg/kg $CuCl_2$ and imaging using Ctrl-PACu-1 (50 μM) ($n = 4$). (*C*) Representative PA images of the liver (dashed white line) for each condition. Liver ROIs are for visualization purposes and were not used for quantification. Values are reported as mean ± SD. Statistical analyses were performed using the Kruskal–Wallis test; $*P < 0.05$.

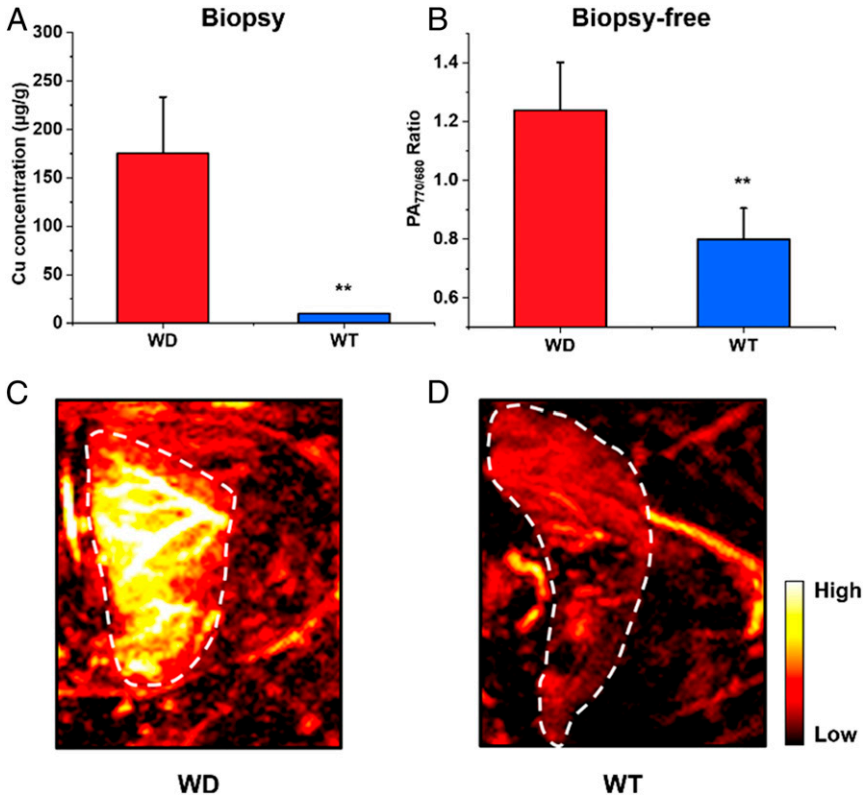

Fig. 4. (*A*) Cu concentration in the liver of WD and WT mice ($n = 4$) obtained via ICP-MS. (*B*) PA ratiometric fold turn-on after treatment with PACu-1 (50 μM, 10% dimethylsulfoxide in saline) in live WD ($n = 7$) and WT ($n = 3$) mice. (*C*) Representative PA image of the liver after treatment with PACu-1 (50 μM, 10% dimethylsulfoxide in saline) in live WD or (*D*) WT mice. Liver ROIs are for visualization purposes and were not used for quantification. Values are reported as mean ± SD. Statistical analyses were performed using the Student's *t* test; $^{**}P < 0.01$.

To this end, we designed a blind experiment in which one investigator randomly selected mice belonging to either the WD or WT groups (eight total) (Fig. 5*A*). Each of the animals were then tagged, and their identities were concealed until the completion of the study. A second investigator then administered PACu-1 and employed PA imaging to identify the WD mice. Notably, there

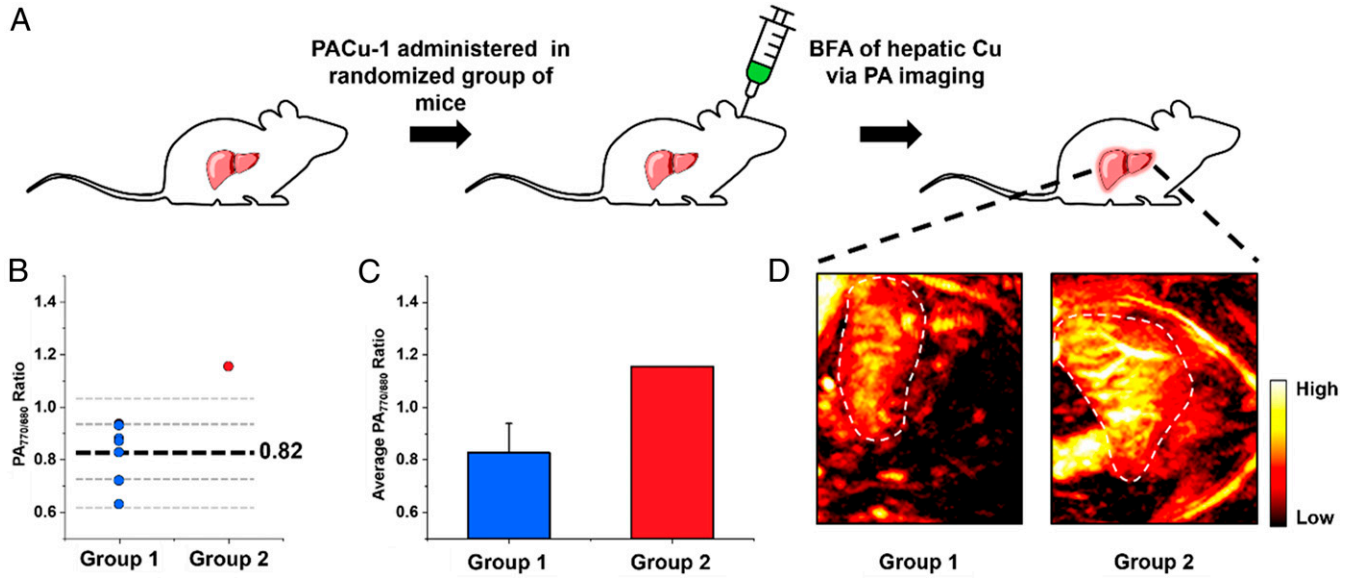

Fig. 5. (*A*) General schematic depicting experimental setup of the blind imaging study. (*B*) PA ratiometric fold turn-on using PACu-1 stratified into Groups 1 and 2 based on diagnostic threshold. Total mice in the blind study were 8 (WT = 7, WD = 1). (*C*) Average PA ratiometric fold turn-on shown in *B*. (*D*) Representative PA images of livers (white dashed line) in Groups 1 and 2. Liver ROIs are for visualization purposes and were not used for quantification. Values are reported as mean ± SD.

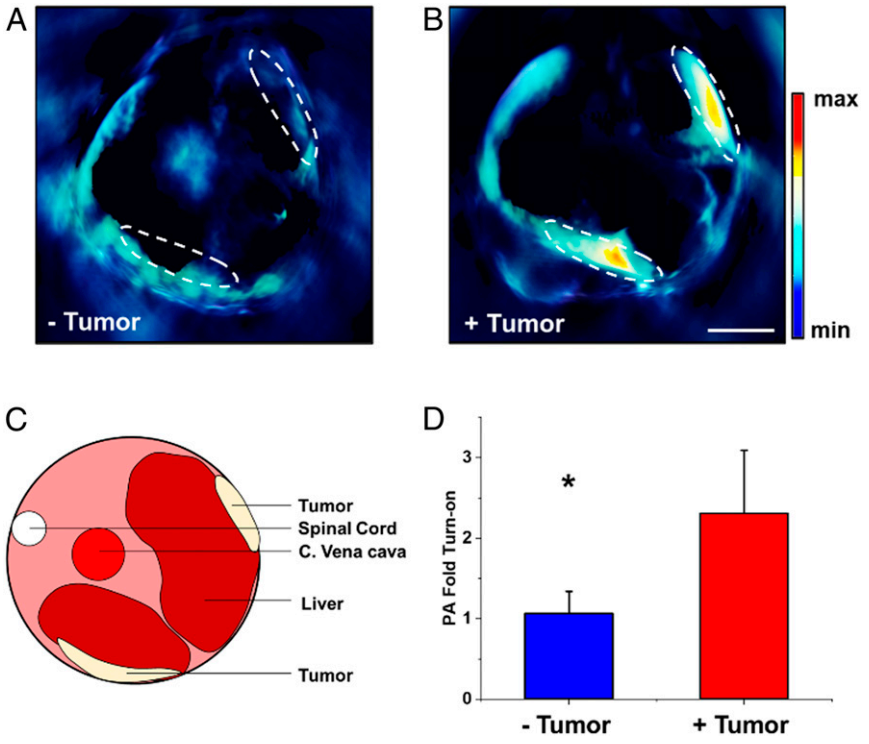

Fig. 6. (*A*) Cross section schematic of a mouse to reference the positioning of the liver and tumor. Representative spectrally unmixed MSOT images of the liver 1 h postinjection in (*B*) non-tumor-bearing mice and (*C*) tumor-bearing mice. (Scale bar, 5 mm.) (*D*) Average PA signal from MSOT imaging represented in *B* ($n = 3$) and *C* ($n = 5$). Statistical analysis was performed using the Student's *t* test; $*P < 0.05$.

were no physical indicators that would allow us to distinguish the mice based on appearance. Prior to BFA, a reliable diagnostic threshold was determined in WT mice, which is defined as the $PA_{770/680}$ ratio (0.82 ± 0.10) (vide infra). With this in mind, we identified seven animals with a $PA_{770/680}$ ratio (0.63, 0.72, 0.82, 0.86, 0.87, 0.93, and 0.94) within the diagnostic threshold (0.82 ±2 SD), which were assigned to Group 1 (WT mice) (Fig. 5 *B–D*). In contrast, only one of the animals had a $PA_{770/680}$ ratio (1.16) greater than three SDs of the diagnostic threshold and was correspondingly assigned to Group 2 (WD mouse). When the identities of the eight animals were revealed at the end of the study, we were able to correctly identify the WD mouse and the WT controls (8/8) with greater than 99.7% confidence. Since there was only one animal in the WD group, we decided to design a second blind experiment, which entailed utilizing PACu-1 to stratify a group of 12 mice consisting of six WD and six WT animals. Based on the performance of PACu-1 and the results from the first blind study, we hypothesized that the six animals with the highest liver PA signals would be WD mice. As before, each of the animals were tagged, randomized, and their identities were concealed. For this experiment, we elected to use the MSOT inVision 128 imaging system (iThera Medical), which is capable of whole-body cross-sectional imaging as well as spectral unmixing to distinguish the signals from PACu-1, its turned-over product, and blood. The six animals with the lowest PA fold turn-on (defined as $PA_{Final}/PA_{Initial}$) (1.00, 1.00, 1.12, 1.19, 1.20, and 1.31) were assigned to Group 1, which we predicted to be WT animals. The second group, which we projected to be WD mice, exhibited a significantly higher PA fold turn-on (1.71, 1.73, 1.92, 1.98, 2.00, and 2.17). Similar to the results obtained from the first blind experiment, we were again able to correctly identify each mouse using PACu-1 (12/12) (*SI Appendix*, Fig. S10 *A* and *B*).

PA Imaging of Cu(I) in a Liver Metastasis Model. Finally, we turned our attention to a second model to further showcase the potential clinical impact of PACu-1. Elevated Cu in cancer of the bone, breast, gastrointestinal tract, and lungs has been associated with aggressive phenotypes and poorer prognosis (31). There are ongoing efforts to employ Cu chelation therapy to reduce the copper status in primary tumors, as well as in metastatic lesions, to treat cancer (52, 53). Since the liver is one of the most common sites of metastasis in the body, BFA of Cu(I) levels would facilitate real-time monitoring during tumor progression and treatment with a chelator. Nu/J mice were either implanted with A549 cells in the liver or received sham surgeries. After 4 wk, PACu-1 was administered for PA imaging using the MSOT system. Compared to the animals that received sham surgeries (1.06 ± 0.28), the PA fold turn-on (after spectral unmixing) for the tumor-bearing mice was 2.31 ± 0.78 (Fig. 6 *A–C*). This indicates that in addition to being able to sense hepatic Cu(I) in WD, PACu-1 can also detect elevated Cu in a lung cancer liver metastasis model.

Discussion

One of the major goals of molecular imaging research is to develop high-performance chemical tools that can noninvasively detect and monitor disease biomarkers in a deep-tissue context. PA imaging is ideal for this application because it involves the conversion of safe near-infrared light to nontoxic ultrasound waves. Since sound at clinically relevant frequencies can readily pass through the body, it is possible to obtain high-resolution images beyond 10 cm in depth (54). Despite the emergence of various acoustogenic probes for analyte sensing, none have been explored to date for BFA of disease biomarkers of the liver. Thus, our goal is to develop PA probes that can potentially replace or complement invasive biopsies currently in use to provide real-time monitoring capabilities.

In this study, we chose to target Cu because, while it is an essential metal ion required by all living organisms, aberrant levels are linked to genetic disorders such as WD as well as most solid cancer types. Our group has previously developed several PA

probes for Cu(II) (16, 38); however, we found that they were not stable when incubated with rat liver microsomes. Likewise, after synthesizing RPS1, a PA probe designed to image Cu(II) in a murine Alzheimer's disease model (39), we discovered that it could not detect exogenous copper in the liver (*SI Appendix*, Fig. S11). These results are not surprising, since each of these examples were designed to respond to Cu in its +2 oxidation state. PACu-1, on the other hand, is highly selective for Cu(I), affords a robust PA signal enhancement when irradiated at 770 nm, is compatible with ratiometric sensing, intrinsically targets the liver, and, most importantly, exhibits an exceptional safety profile.

It is worth noting that one of the major differences between BFA using PACu-1 and traditional biopsies is that our probe is designed to detect the labile Cu pool (Cu associated with GSH), whereas the latter technique reports on the total Cu content in the sample. Despite this difference, we can still reliably distinguish WD mice from WT controls, as shown in our two blind studies. Moreover, although we did not intentionally include only one WD animal in our first BFA experiment, we were satisfied with the outcome because WD occurs in approximately one in 30,000 to 40,000 people worldwide. Therefore, a study with fewer subjects with WD is more representative compared to a scenario in which the numbers are closer to parity. Despite this, we designed and successfully executed a second BFA experiment in which the goal was to use PACu-1 to stratify six WD and six WT mice based on their liver PA signals. In addition to detecting Cu in WD, we also demonstrate that PACu-1 can be used to assess elevated Cu in a liver metastasis model. We envision that PACu-1 can be used to aid in the development of new Cu chelators or in conjunction with existing Cu binding drugs to monitor changes in real time. As previously mentioned, we employed two different PA instruments for the WD and cancer studies. This indicates that PACu-1 will be compatible with a range of imaging systems including new handheld scanners (55, 56), wearable devices (57, 58), and endoscopic setups (59, 60).

Materials and Methods

In Vitro Selectivity Assay. The initial absorbance (400 to 800 nm) of PACu-1 (5 μM, 1:1 vol/vol dimethylformamide:Hepes, pH 7.4) was measured before the addition of a panel of metal ions (100 μM). These initial measurements were used to determine the initial ratio$_{770/680}$ via UV-vis (ultraviolet-visible) spectroscopy. After addition, the cuvette was sealed and incubated for 1 h. Final measurements were recorded, and the ratiometric fold turn-on was calculated by dividing the final ratio by the initial ratio. All metal solutions were prepared in water from their chloride salt except for Ag_2CO_3, Cs_2CO_3, and tetrakis(acetonitrile)copper(I) hexafluorophosphate.

Live-Subject Statement. All animal experiments were performed with the approval of the Institutional Animal Care and Use Committee (IACUC) of the University of Illinois at Urbana–Champaign, following the principles outlined by the American Physiological Society on research animal use.

Biopsy Assessment of Hepatic Cu via ICP-MS. BALB/c mice were anesthetized using isoflurane (1.5 to 2.0%). The mice were then intraperitoneally injected with a solution of $CuCl_2$ (5 mg/kg) or vehicle (sterilized saline). After 2 h, the mice were killed, and then the liver was excised and weighed for ICP-MS analysis. The 2-h incubation time was used to reduce Cu in vivo. To determine the Cu concentration in WT (B6129SF2/J) and WD (B6;129S1-*Atp7b*^{tm1Tcg}/LtsnkJ) mice, the livers were similarly prepared as the BALB/c mice for ICP-MS analysis, except no intraperitoneal injections were performed.

Ex Vivo Biodistribution of PACu-1 via PA Imaging. BALB/c mice were anesthetized using isoflurane (1.5 to 2.0%) and retro-orbitally injected with either a solution of PACu-1 (50 μM) or vehicle (10% dimethylsulfoxide in sterilized saline, 50 μL). After 1 h, the mice were killed, and the liver, spleen, heart, and kidneys were excised. Photoacoustic imaging of the organs was performed at 680 and 770 nm using continuous mode with a 6-s rotation time (Nexus 128+, Endra Life Sciences). The ratio of the PA signals in PACu-1–treated mice obtained upon excitation at 680 nm and 770 nm was normalized to the ratio of the PA signals in vehicle-treated mice.

Determination of the Diagnostic Threshold. A group of 10 WT mice (B6129SF2/J), which are direct controls of the WD mice (B6;129S1-*Atp7b*^{tm1Tcg}/LtsnkJ), were used to determine the diagnostic threshold for hepatic Cu in WD via PA imaging. After the mice were anesthetized using isoflurane (1.5 to 2.0%), their abdomens were shaved, and they were positioned in the PA tomographer to facilitate direct imaging of the abdomen. After an image was acquired, an ROI (region of interest) was drawn around the liver to determine the signal intensity. The ratio of the PA signals obtained upon excitation at 680 nm and 770 nm in the ROI provided the initial PA$_{770/680}$ ratio. The mice were then treated with a 50-μM solution of PACu-1 in saline containing 10% dimethylsulfoxide (50 μL) via retro-orbital injection. The mice were returned to their cages for 60 min while PACu-1 was allowed to react with the hepatic Cu. The mice were anesthetized, and their livers were imaged as described previously to obtain the final PA$_{770/680}$ ratio. The diagnostic threshold value (mean ± 2 × SD) was determined by dividing the final PA$_{770/680}$ ratio with the initial PA$_{770/680}$ ratio.

Identification of WD via PA Imaging in Blind Study No. 1. A group of eight mice consisting of one WD animal (B6;129S1-*Atp7b*^{tm1Tcg}/LtsnkJ) and seven WT animals (B6129SF2/J mice) was tagged and randomized by the first researcher. Their identity and the total number of WD mice present were concealed until the end of the study. Importantly, these mice had no distinguishing physical features that would allow us to identify them based on appearance. PA imaging of hepatic Cu using PACu-1 was then performed by a second researcher to determine the PA ratiometric fold turn-on for each animal. Mice with a PA$_{770/680}$ ratio value greater than 1.02 were assigned to Group 1 (WD), and mice with a PA$_{770/680}$ ratio value between 0.62 and 1.02 were assigned to Group 2 (WT). After PA imaging was performed on all animals, the assignment and identity were revealed to and validated by the corresponding author.

Stratification of WD and WT Mice via PA Imaging in Blind Study No. 2. A group of 12 mice consisting of six WD animals (B6;129S1-*Atp7b*^{tm1Tcg}/LtsnkJ) and six WT animals (B6129SF2/J mice) was tagged and randomized by the first researcher. Their identity was concealed until the end of the study. A second researcher used a MSOT PA imaging system to identify the six WD animals based on the highest liver PA signals. Likewise, the six animals with the lowest liver PA signals were assigned to the WT group. The results were revealed by the corresponding author with both researchers present.

Statistical Analyses. Statistical analyses were performed in Microsoft Excel. Sample sizes in all experiments were sufficiently powered to detect at least a P value < 0.05, which was significant. All data are expressed as mean ± SD. Multiple group analysis was performed using the Kruskal–Wallis Test. All other in vivo imaging data were analyzed by performing the Student's t test ($\alpha = 0.05$). $^*P > 0.05$; $^{**}P > 0.01$.

Data Availability. All study data are included in the article and/or *SI Appendix*.

ACKNOWLEDGMENTS. M.Y.L. thanks the Alfred P. Sloan Foundation and the Pines Graduate Fellowship for financial support. Major funding for the 500-MHz Bruker CryoProbe was provided by the Roy J. Carver Charitable Trust (Grant No. 15-4521) to the School of Chemical Sciences NMR Lab. The Q-Tof Ultima mass spectrometer was purchased in part with a grant from the NSF, Division of Biological Infrastructure (DBI-0100085). We also acknowledge Dr. Iwona Dobrucka and the Molecular Imaging Laboratory at the Beckman Institute for use of the IVIS imaging system, the veterinary histology, and diagnostic laboratories for performing H&E staining and liver function tests, Drs. Nicole Herndon and Jessica Xu for help generating the liver metastasis model, and Prof. Svetlana Lutsenko for helpful discussions. This work was supported in part by the NSF (1752879).

1. I. Steinberg *et al.*, Photoacoustic clinical imaging. *Photoacoustics* **14**, 77–98 (2019).
2. A. B. E. Attia *et al.*, A review of clinical photoacoustic imaging: Current and future trends. *Photoacoustics* **16**, 100144 (2019).
3. L. V. Wang, S. Hu, Photoacoustic tomography: In vivo imaging from organelles to organs. *Science* **335**, 1458–1462 (2012).
4. A. K. East, M. Y. Lucero, J. Chan, New directions of activity-based sensing for *in vivo* NIR imaging. *Chem. Sci. (Camb.)* **12**, 3393–3405 (2020).
5. Y. Liu *et al.*, Recent advances in organic-dye-based photoacoustic probes for biosensing and bioimaging. *Sci. China Chem.* **62**, 1275–1285 (2019).
6. J. Chan, S. C. Dodani, C. J. Chang, Reaction-based small-molecule fluorescent probes for chemoselective bioimaging. *Nat. Chem.* **4**, 973–984 (2012).
7. K. J. Bruemmer, S. W. M. Crossley, C. J. Chang, Activity-based sensing: A synthetic methods approach for selective molecular imaging and beyond. *Angew. Chem. Int. Ed. Engl.* **59**, 13734–13762 (2020).

8. S. H. Gardner, C. J. Reinhardt, J. Chan, Advances in activity-based sensing probes for isoform-selective imaging of enzymatic activity. *Angew. Chem. Int. Ed. Engl.* **60**, 5000–5009 (2021).
9. L. Yin *et al*., Quantitatively visualizing tumor-related protease activity in vivo using a ratiometric photoacoustic probe. *J. Am. Chem. Soc.* **141**, 3265–3273 (2019).
10. Y. Wang *et al*., A photoacoustic probe for the imaging of tumor apoptosis by caspase-mediated macrocyclization and self-assembly. *Angew. Chem. Int. Ed. Engl.* **58**, 4886–4890 (2019).
11. P. Cheng *et al*., Fluoro-photoacoustic polymeric renal reporter for real-time dual imaging of acute kidney injury. *Adv. Mater.* **32**, e1908530 (2020).
12. Y. Wu *et al*., Activatable probes for diagnosing and positioning liver injury and metastatic tumors by multispectral optoacoustic tomography. *Nat. Commun.* **9**, 3983 (2018).
13. H. J. Knox *et al*., A bioreducible N-oxide-based probe for photoacoustic imaging of hypoxia. *Nat. Commun.* **8**, 1794 (2017).
14. H. J. Knox, T. W. Kim, Z. Zhu, J. Chan, Photophysical tuning of N-oxide-based probes enables ratiometric photoacoustic imaging of tumor hypoxia. *ACS Chem. Biol.* **13**, 1838–1843 (2018).
15. M. Chen *et al*., Simultaneous photoacoustic imaging of intravascular and tissue oxygenation. *Opt. Lett.* **44**, 3773–3776 (2019).
16. H. Li, P. Zhang, L. P. Smaga, R. A. Hoffman, J. Chan, Photoacoustic probes for ratiometric imaging of copper(II). *J. Am. Chem. Soc.* **137**, 15628–15631 (2015).
17. C. J. Reinhardt, E. Y. Zhou, M. D. Jorgensen, G. Partipilo, J. Chan, A ratiometric acoustogenic probe for in vivo imaging of endogenous nitric oxide. *J. Am. Chem. Soc.* **140**, 1011–1018 (2018).
18. C. J. Reinhardt, R. Xu, J. Chan, Nitric oxide imaging in cancer enabled by steric relaxation of a photoacoustic probe platform. *Chem. Sci. (Camb.)* **11**, 1587–1592 (2020).
19. J. Zhang *et al*., Activatable photoacoustic nanoprobes for in vivo ratiometric imaging of peroxynitrite. *Adv. Mater.* **29**, 1604764 (2017).
20. S. Roberts *et al*., Calcium sensor for photoacoustic imaging. *J. Am. Chem. Soc.* **140**, 2718–2721 (2018).
21. C. Zhang *et al*., Design and synthesis of a ratiometric photoacoustic probe for in situ imaging of zinc ions in deep tissue in vivo. *Anal. Chem.* **92**, 6382–6390 (2020).
22. M. Y. Lucero, J. Chan, Towards personalized medicine: Photoacoustic imaging of glutathione enables companion diagnosis and targeted treatment of lung cancer. *ChemRxiv*. [Preprint] (2020). https://doi.org/10.26434/chemrxiv.11888214.v2. Accessed 3 July 2021.
23. M. Y. Lucero *et al*., Development of NIR-II photoacoustic probes tailored for deep-tissue sensing of nitric oxide. *J. Am. Chem. Soc.* **143**, 7196–7202 (2021).
24. S. H. Gardner *et al*., A general approach to convert hemicyanine dyes into highly optimized photoacoustic scaffolds for analyte sensing. *Angew. Chem. Int. Ed.* **60**, 18860 (2021).
25. A. I. Tobkes, H. J. Nord, Liver biopsy: Review of methodology and complications. *Dig. Dis.* **13**, 267–274 (1995).
26. S. Oe *et al*., Importance of a liver biopsy in the management of Wilson disease. *Intern. Med.* **59**, 77–81 (2020).
27. L. Di Tommaso *et al*., Role of liver biopsy in hepatocellular carcinoma. *World J. Gastroenterol.* **25**, 6041–6052 (2019).
28. P. Ferenci, Review article: Diagnosis and current therapy of Wilson's disease. *Aliment. Pharmacol. Ther.* **19**, 157–165 (2004).
29. D. Huster *et al*., Consequences of copper accumulation in the livers of the Atp7b-/- (Wilson disease gene) knockout mice. *Am. J. Pathol.* **168**, 423–434 (2006).
30. I. Yücel *et al*., Serum copper and zinc levels and copper/zinc ratio in patients with breast cancer. *Biol. Trace Elem. Res.* **40**, 31–38 (1994).
31. V. C. Shanbhag *et al*., Copper metabolism as a unique vulnerability in cancer. *Biochim. Biophys. Acta Mol. Cell Res.* **1868**, 118893 (2021).
32. S. Adachi, K. Takemoto, S. Ohshima, Y. Shimizu, M. Takahama, Metal concentrations in lung tissue of subjects suffering from lung cancer. *Int. Arch. Occup. Environ. Health* **63**, 193–197 (1991).
33. X. Zhang, Q. Yang, Association between serum copper levels and lung cancer risk: A meta-analysis. *J. Int. Med. Res.* **46**, 4863–4873 (2018).
34. J. A. Cotruvo Jr, A. T. Aron, K. M. Ramos-Torres, C. J. Chang, Synthetic fluorescent probes for studying copper in biological systems. *Chem. Soc. Rev.* **44**, 4400–4414 (2015).
35. C. M. Ackerman, S. Lee, C. J. Chang, Analytical methods for imaging metals in biology: From transition metal metabolism to transition metal signaling. *Anal. Chem.* **89**, 22–41 (2017).
36. T. Hirayama, G. C. Van de Bittner, L. W. Gray, S. Lutsenko, C. J. Chang, Near-infrared fluorescent sensor for in vivo copper imaging in a murine Wilson disease model. *Proc. Natl. Acad. Sci. U.S.A.* **109**, 2228–2233 (2012).
37. M. C. Heffern *et al*., In vivo bioluminescence imaging reveals copper deficiency in a murine model of nonalcoholic fatty liver disease. *Proc. Natl Acad. Sci. U. S. A.* **113**, 14219–14224 (2016).
38. E. Y. Zhou, H. J. Knox, C. Liu, W. Zhao, J. Chan, A conformationally restricted Aza-BODIPY platform for stimulus-responsive probes with enhanced photoacoustic properties. *J. Am. Chem. Soc.* **141**, 17601–17609 (2019).
39. S. Wang *et al*., Activatable small-molecule photoacoustic probes that cross the blood-brain barrier for visualization of copper(II) in mice with Alzheimer's disease. *Angew. Chem. Int. Ed. Engl.* **58**, 12415–12419 (2019).
40. R. A. Festa, D. J. Thiele, Copper: An essential metal in biology. *Curr. Biol.* **21**, R877–R883 (2011).
41. M. Taki, S. Iyoshi, A. Ojida, I. Hamachi, Y. Yamamoto, Development of highly sensitive fluorescent probes for detection of intracellular copper(I) in living systems. *J. Am. Chem. Soc.* **132**, 5938–5939 (2010).
42. W. T. Eckenhoff, T. Pintauer, Structural comparison of copper(I) and copper(II) complexes with tris(2-pyridylmethyl)amine ligand. *Inorg. Chem.* **49**, 10617–10626 (2010).
43. A. Kunishita *et al*., H_2O_2-reactivity of copper(II) complexes supported by tris[(pyridin-2-yl) methyl]amine ligands with 6-phenyl substituents. *Inorg. Chem.* **47**, 12032–12039 (2008).
44. E. Y. Zhou *et al*., Near-infrared photoactivatable nitric oxide donors with integrated photoacoustic monitoring. *J. Am. Chem. Soc.* **140**, 11686–11697 (2018).
45. S. C. Lu, Dysregulation of glutathione synthesis in liver disease. *Liver Res.* **4**, 64–73 (2020).
46. N. Traverso *et al*., Role of glutathione in cancer progression and chemoresistance. *Oxid. Med. Cell. Longev.* **2013**, 972913 (2013).
47. I. B. Butler, M. A. A. Schoonen, D. T. Rickard, Removal of dissolved oxygen from water: A comparison of four common techniques. *Talanta* **41**, 211–215 (1994).
48. H. Y. Au-Yeung, E. J. New, C. J. Chang, A selective reaction-based fluorescent probe for detecting cobalt in living cells. *Chem. Commun. (Camb.)* **48**, 5268–5270 (2012).
49. H. Y. Au-Yeung, J. Chan, T. Chantarojsiri, C. J. Chang, Molecular imaging of labile iron(II) pools in living cells with a turn-on fluorescent probe. *J. Am. Chem. Soc.* **135**, 15165–15173 (2013).
50. H. M. Alvarez *et al*., Tetrathiomolybdate inhibits copper trafficking proteins through metal cluster formation. *Science* **327**, 331–334 (2010).
51. J. Ludwig, T. P. Moyer, J. Rakela, The liver biopsy diagnosis of Wilson's disease. Methods in pathology. *Am. J. Clin. Pathol.* **102**, 443–446 (1994).
52. G. Khan, S. Merajver, Copper chelation in cancer therapy using tetrathiomolybdate: An evolving paradigm. *Expert Opin. Investig. Drugs* **18**, 541–548 (2009).
53. S. Baldari, G. Di Rocco, G. Toietta, Current biomedical use of copper chelation therapy. *Int. J. Mol. Sci.* **21**, 1069 (2020).
54. U. Chitgupi *et al*., Surfactant-stripped micelles for NIR-II photoacoustic imaging through 12 cm of breast tissue and whole human breasts. *Adv. Mater.* **31**, e1902279 (2019).
55. Y.-H. Liu, Y. Xu, L.-D. Liao, K. C. Chan, N. V. Thakor, A handheld real-time photoacoustic imaging system for animal neurological disease models: From simulation to realization. *Sensors (Basel)* **18**, 4081 (2018).
56. A. Taruttis *et al*., Optoacoustic imaging of human vasculature: Feasibility by using a handheld probe. *Radiology* **281**, 256–263 (2016).
57. J. Yao, L. V. Wang, Photoacoustic brain imaging: From microscopic to macroscopic scales. *Neurophotonics* **1**, 011003 (2014).
58. J. Tang, J. E. Coleman, X. Dai, H. Jiang, Wearable 3-D photoacoustic tomography for functional brain imaging in behaving rats. *Sci. Rep.* **6**, 25470 (2016).
59. J.-M. Yang *et al*., A 2.5-mm diameter probe for photoacoustic and ultrasonic endoscopy. *Opt. Express* **20**, 23944–23953 (2012).
60. J.-M. Yang *et al*., Simultaneous functional photoacoustic and ultrasonic endoscopy of internal organs in vivo. *Nat. Med.* **18**, 1297–1302 (2012).